

Structural Properties of NdTiO₂N and Its Application as Photoanode

Zili Ma^{a,b,†,*}, Kaixuan Chen^{a,†}, Aleksander Jaworski^b, Anna Rokicinska^c, Piotr Kuśtrowski^c, Richard Dronskowski^{a,d}, Adam Slabon^{b,*}

^a *Institute of Inorganic Chemistry, RWTH Aachen University, 52056 Aachen, Germany*

^b *Department of Materials and Environment Chemistry, Stockholm University, Svante Arrhenius väg 16 C, 106 91 Stockholm, Sweden*

^c *Faculty of Chemistry, Jagiellonian University, Gronostajowa 2, 30-387 Krakow, Poland*

^d *Hoffmann Institute of Advanced Materials, Shenzhen Polytechnic, 7098 Liuxian Blvd, Nanshan District, Shenzhen, China*

† These authors contributed equally to this paper.

**Corresponding author.*

E-mail address: adam.slabon@mmk.su.se (A. Slabon)

E-mail address: zili.ma@ac.rwth-aachen.de (Z. Ma)

ABSTRACT

Mixed-anion inorganic compounds offer diverse functionalities as a function of the different physicochemical characteristics of the secondary anion. The quaternary metal oxynitrides, which originate from substituting oxygen anions (O²⁻) in a parent oxide by nitrogen (N³⁻), are encouraging candidates for photoelectrochemical (PEC) water splitting owing to their suitable and adjustable narrow band gap and relative negative conduction band (CB) edge. Given the known photochemical activity of LaTiO₂N, we investigated the paramagnetic counterpart NdTiO₂N. The electronic structure was explored both experimentally and theoretically at the density-functional theory (DFT) level. A band gap (E_g) of 2.04 eV was determined by means of Ultraviolet-visible (UV-vis) spectroscopy, and a relative negative flat band potential of -0.33 V vs. reversible hydrogen electrode (RHE) was proposed via Mott–Schottky measurements. ¹⁴N solid state nuclear magnetic resonance (NMR) signals from NdTiO₂N could not be detected,

which indicates that NdTiO₂N is berthollide, in contrast to other structurally related metal oxynitrides. Although the bare particle-based photoanode did not exhibit noticeable photocurrent, Nb₂O₅ and CoO_x overlayers were deposited to extract holes and activate NdTiO₂N. Multiple electrochemical methods were employed to understand the key features required for this metal oxynitride in order to fabricate photoanodes.

Keywords: Mixed-anion; Photoelectrochemistry; Water splitting; Solid-state NMR spectroscopy; DFT

1. Introduction

The globally increasing energy demand, which has been mostly met by fossil fuels up to now, is an important challenge. Developing generation-IV nuclear technology of high energy density in combination with “renewable” energy of lower density is currently considered a promising strategy for matching that challenge. With respect to the utilization of solar energy to produce alternative fuels, photoelectrochemical (PEC) technology looks like a sustainable solution by splitting water into “green” energy carrier hydrogen under sunlight irradiation, irrespective of the additional challenge to store and ship hydrogen.[1] To improve the efficiency of PEC cells, attempts have been extensively explored since the pioneering conception of water splitting over semiconducting TiO₂. [2]

Serving as the core components of a PEC cell, the semiconducting photoelectrodes responsible for capturing energy from sunlight drive the separation of holes and electrons for consecutive oxidation and reduction of water. The slow kinetics of the oxygen evolution reaction (OER) over n-type photoanodes has motivated scientists to explore materials to address these pivotal issues.[3] The most investigated n-type oxide-based semiconductors have, however, a more positive conduction band (CB) edge than the reduction potential for H⁺/H₂, resulting in a high overpotential for OER.[4] Hence,

the relatively positive CB position inherently requires more external bias to realize PEC water splitting.

Beyond metal oxides, mixed-anion inorganic compounds, such as oxyfluorides, oxynitrides, oxide-carbodiimides, oxysulfides, oxyhalides, and oxyhydrides could offer diverse functionalities originating from the different properties of the secondary anion.[5–8] Within the recent two decades, transition-metal oxynitrides have emerged as promising photoactive materials due to their frequently higher theoretical solar-to-hydrogen efficiency. This is in particular promising for the quaternary metal oxynitrides, because they can exhibit a smaller band gap than the binary Ta_3N_5 ($E_g = 2.1$ eV). The less electronegative element N and its more covalent interaction with the metal orbitals as compared to the O 2p orbitals induces an upward shift of the valence band (VB) in such compounds, resulting in higher light absorption capability toward the wide visible range.[9–11] Domen et al. have demonstrated a niobium-based oxynitride $BaNbO_2N$ photoanode with photoexcitation up to 740 nm.[12] It should be noted that different anion ordering will affect the band gap varying up to 0.6 eV, which was proven previously on the example of $CaTaO_2N$. [13] The proper band edge positions of quaternary oxynitrides generally straddle the redox potential of water, thereby making them promising visible light-induced photoelectrodes for overall water splitting.[14] Their negative CB edge positions give negative photocurrent onset potential, which makes metal oxynitrides also potentially interesting for the reduction of CO_2 or N_2 . [15–17]

The quaternary metal oxynitrides of general formula $AB(O,N)_3$ (A = alkaline-earth metal, lanthanide; B = Ta, Nb, Ti) can exhibit different properties depending on their chemical composition. They are part of a large perovskite-like class of compounds whose synthesis, characterization, properties, and theory have been reviewed quite a

while ago.[18] The alkaline-earth metal tantalum-based oxynitrides CaTaO_2N , SrTaO_2N and BaTaO_2N crystallize in different space-group symmetries, i.e. orthorhombic, tetragonal, cubic, as a result of the structural distortion factor caused by the cation radius,[9]; in contrast to that *averaged* structural description by X-ray diffraction which always suffers from the tiny scattering contrast between N and O, there are strong indications, both from first-principles electronic-structure calculations as well as molecular-dynamics simulations, that the *local* site symmetries are lower, for example corresponding to orthorhombic symmetry for all the three compounds throughout, including their niobium-based counterparts.[18,19] While their conduction band edge positions differ up to 0.82 eV, the bottom of the conduction band has been proposed to consist entirely of empty Ta 5d orbitals, not too surprising for pentavalent tantalum.[9,20] In comparison to tantalum-based and niobium-based oxynitrides, the titanium-based quaternary oxynitrides, except LaTiO_2N , have rarely been investigated for PEC applications.[21] A study by Woodward et al. has shown that NdTiO_2N and LaTiO_2N crystallize in different space groups but exhibit similar photocatalytic activity for water splitting which is better than for CeTiO_2N and PrTiO_2N . [22] Since the PEC performance is sensitive to the band alignment of the CB and VB edges with respect to the water redox potentials, we were interested to investigate the structural properties of NdTiO_2N and explore its PEC water splitting activity.

2. Experimental

2.1. Synthesis of NdTiO_2N

The $\text{Nd}_2\text{Ti}_2\text{O}_7$ oxide precursor was conventionally synthesized by solid-state reaction (SSR) with KCl as a flux. In a typical synthesis, 1.5 mmol of Nd_2O_3 (99.999 wt %, Koch-Light Laboratories Ltd), 3 mmol of TiO_2 (99.3 wt %, VWR Chemicals)

and 15 mmol of KCl (99.5 wt %, Grüssing GmbH) were mixed and ground, followed by heating in air at 1423 K for 8 hours. The product was cooled to room temperature and washed thoroughly with distilled water to remove residual flux. The dried $\text{Nd}_2\text{Ti}_2\text{O}_7$ precursor was placed into an alumina crucible and put in a tube furnace. The thermal ammonolysis was carried out under a constant flow of NH_3 (15 mL min^{-1}) and H_2 (5 mL min^{-1}) at 1223 K for 15 h at a ramping rate of 10 K min^{-1} . This ammonolysis process was repeated three times with intermittent grindings.[22]

2.2. Fabrication of NdTiO_2N photoanodes

The NdTiO_2N powder was assembled into a thin film on pre-cleaned conductive fluorine-doped tin oxide (FTO) glass (2.2 mm thick, Sigma-Aldrich) via an electrophoretic deposition process. Concisely, 20 mg of NdTiO_2N were dispersed in 30 ml of acetone containing 10 mg of iodine by 20 min sonication to obtain a uniform suspension. Two FTO slides were immersed into the suspension parallelly with about 10 mm gap, then a 35 V bias was applied between them for 1 min. The FTO/ NdTiO_2N photoanodes were dried naturally in air.

A NbCl_5 impregnation step, which was adapted from TaCl_5 and TiCl_4 , [15,23] was performed to improve the connection of particles. The FTO/ NdTiO_2N photoelectrode was soaked in 0.1 M NbCl_5 (99.99 wt %, abcr GmbH) dissolved in ethanol for 10 seconds, and dried on a hot plate at 423 K. After repeating this procedure for four rounds, the electrode was then annealed in air at 573 K for 1 hour to get FTO/ $\text{NdTiO}_2\text{N}/\text{Nb}_2\text{O}_5$. The electrode was further decorated with a water oxidation cocatalyst, i.e. CoO_x . 45 μL of 7 mM $\text{Co}(\text{NO}_3)_2$ dissolved in methanol were dropped on the FTO/ $\text{NdTiO}_2\text{N}/\text{Nb}_2\text{O}_5$ surface followed by annealing at 473 K for 1 hour. The composite electrode was washed with distilled water.

2.3. Characterization

Powder X-ray diffraction (PXRD) patterns were recorded in the transmission mode on a STOE STADI-P diffractometer (Cu $K\alpha_1$ radiation) equipped with a DECTRIS Mythen 1K detector. UV-vis spectrophotometer (UV-2600, Shimadzu) was employed to characterize the optical properties using $BaSO_4$ as the reference. The IR spectrums were acquired via a Nicolet Avatar 369 FT-IR spectrometer (Thermo Fisher Scientific, USA) using KBr as the reference. Scanning electron microscopy (SEM) images were collected via a Leo Supra 35VP SMT (Zeiss). X-ray photoelectron spectroscopy (XPS) measurements were performed in a Prevac photoelectron spectrometer, an essential part of which was a hemispherical analyzer (VG SCIENTA R3000). The spectra were collected using a monochromatized aluminum source Al $K\alpha$ ($E = 1486.6$ eV) with no charge compensation. The C 1s reference peak at 285.0 eV (typical of C-C bonds) was used for calibration of binding energy scale. The composition and chemical state were determined by analysis of areas and binding energies of Nd 3d, Nd 4d, Nb 3d, Co 2p, Ti 2p, O 1s, N 1s and C 1s photoelectron peaks. All operations on the experimental data, including fitting the Shirley background and deconvolution with the mixed function of Gauss and Lorentz (GL = 30), were performed in the Casa XPS software.

2.4. Solid-state NMR spectroscopy

Solid-state 1H magic angle spinning (MAS) NMR spectrum was acquired at a magnetic field strength of 14.1 T (Larmor frequency 600.1 MHz) with a Bruker Avance III spectrometer equipped with a 1.3 mm MAS probehead and employing MAS rate of 60.00 kHz. Acquisition involved with rotor-synchronized, double-adiabatic spin-echo sequence with a 90 degree excitation pulse of 1.1 μs , followed by two 50.0 μs tanh/tan short high-power adiabatic pulses with 5 MHz frequency sweep.[24,25] All pulses operated at a nutation frequency of 210 kHz. 256 signal transients with 5 s relaxation delay were accumulated. 1H shifts were referenced using neat tetramethylsilane (TMS).

2.5. Computational methods

First-principles DFT calculations were performed using the Vienna ab-initio simulation package (VASP).[26] Projector-augmented-wave (PAW) potentials with the exchange-correlation functional of Perdew-Burke-Ernzerhof (PBE) were adopted. The plane-wave energy cutoff was set to 600 eV. Meta-generalized gradient approximations (meta-GGA) with the new SCAN functional[27] was used with a Γ -centered Monkhorst-Pack $6 \times 4 \times 6$ k-mesh. Note that the 4f electrons in Nd are treated as core electrons, instead of valence electrons. In the density of states calculation, a denser $8 \times 8 \times 8$ k-mesh was adopted. In addition, the hybrid HSE06 functional was further used to obtain a more accurate band structure.

2.6. Electrochemical measurements

A conventional three-electrode setup was used to perform all the electrochemical measurements in 1 M NaOH electrolyte (pH = 13.6). The FTO slide deposited with NdTiO₂N was used as working electrode with an exposed geometrical surface area of ca. 0.79 cm². Platinum wire and a 1 M Ag/AgCl electrode were used as counter and reference electrodes, respectively. The recorded potential vs 1 M Ag/AgCl was converted subsequently vs RHE according to Nernst equation $E_{\text{RHE}} = E_{1\text{M Ag/AgCl}}^0 + 0.059 \times \text{pH} + E_{\text{Ag/AgCl}}$. The light source was one sun simulated solar irradiation (AM 1.5G, 100 mW cm⁻²) generated by a solar light simulator (class-AAA 94023A, Newport) with an ozone-free 450 W xenon short-arc lamp. Mott–Schottky measurements were conducted using the Gamry INTERFACE 1010T Potentiostat/Galvanostat/ZRA workstation at ac amplitude of 5 mV and different frequencies under dark conditions. The electrochemical impedance spectroscopy (EIS) was measured at 1.0 V vs. RHE in an ac potential frequency range of 20 kHz to 0.2 Hz under an AM 1.5G illumination. The linear square voltammetry (LSV) curves were swept negatively at a scan rate of 10

mV s⁻¹ and chronoamperometry (CA) curves at a constant bias 1.23 V vs RHE were recorded with a potentiostat (PalmSens4, PalmSens BV). Open circuit photovoltages (OCPV) were collected under chopped illumination.

3. Results and discussion

3.1. Structural analysis

The topotactic transformation of oxides via nitridation has been frequently used towards the synthesis of metal oxynitrides, which can enhance the exploitation range of visible light.[28] The PXRD patterns of Nd₂Ti₂O₇ (Fig. 1a) are characteristic of a material belonging to the family of compounds with a non-centrosymmetric structure having perovskite-type slabs (space group *P112₁*).[29] During ammonolysis at high temperature, the Nd₂Ti₂O₇ precursor was converted to an oxynitride through O²⁻/N³⁻ substitution (Fig. 1b). The resulting compound from the ammonolysis was identified as NdTiO₂N by means of PXRD, matching with previous report ICSD 94764 (Fig. 1a).[30] The product crystallizes in a distorted perovskite-related structure (space group *Pnma*).[30]

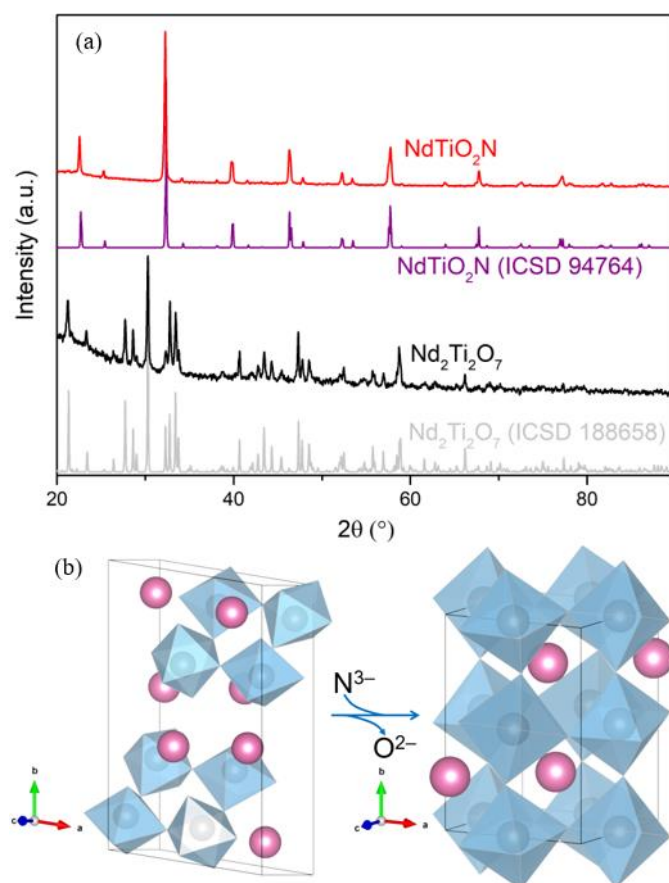


Fig. 1. (a) PXRD pattern of $\text{Nd}_2\text{Ti}_2\text{O}_7$ and NdTiO_2N , for reference the corresponding simulated PXRD patterns are also shown; (b) crystal structural evolution from $\text{Nd}_2\text{Ti}_2\text{O}_7$ to NdTiO_2N through $\text{O}^{2-}/\text{N}^{3-}$ substitution. It should be mentioned that the composition of the ternary metal oxynitride has been previously reported to have an oxygen-rich composition $\text{NdTiO}_{2.17}\text{N}_{0.83}$, with a statistic O/N distribution (*vide infra*).[30]

After chemical conversion from $\text{Nd}_2\text{Ti}_2\text{O}_7$ to NdTiO_2N through $\text{O}^{2-}/\text{N}^{3-}$ substitution, IR spectra have also been conducted to identify the bonding situation. As displayed in Fig. 2a, the oxide precursor $\text{Nd}_2\text{Ti}_2\text{O}_7$ shows a typical spectra shape of lanthanide titanates $\text{Ln}_2\text{Ti}_2\text{O}_7$. [31,32] The broader peaks for the oxynitride NdTiO_2N sample suggest high O/N disorder in the $\text{TiO}_{6-x}\text{N}_x$ octahedra. [30]

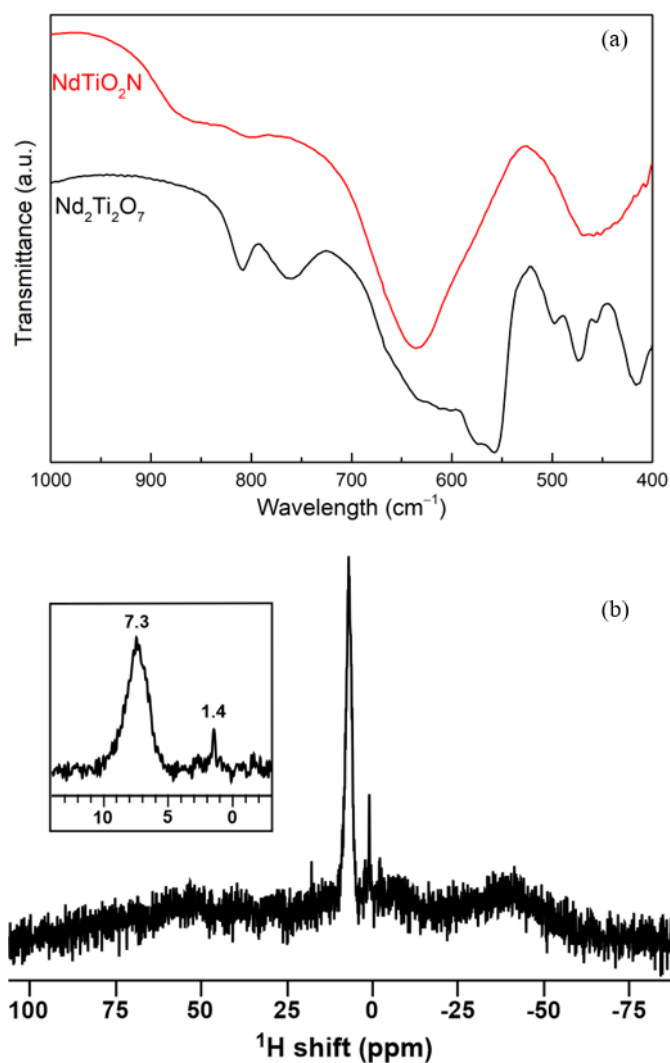


Fig. 2. (a) IR spectra of $\text{Nd}_2\text{Ti}_2\text{O}_7$ and NdTiO_2N and (b) ^1H MAS NMR spectra of NdTiO_2N . The inset shows the zoomed ^1H NMR signal from NdTiO_2N .

In Fig. 2b the ^1H MAS NMR spectrum of NdTiO_2N surface is shown. The proton signals are severely affected by paramagnetic interactions with unpaired electrons of the Nd^{3+} ions. Most of the expected signal intensity is buried in the baseline as a broad, featureless bump. Only two narrow (albeit very weak) signals remain: at 7.3 and 1.4 ppm, which we assign to physisorbed water and hydroxyl groups, respectively. The general appearance of the spectrum is very similar to that collected from CeTiO_2N .^[33] Importantly, in contrast to CeTiO_2N , the ^{14}N NMR signal from NdTiO_2N could not be detected, which we attribute to the fact that NdTiO_2N has a statistic O/N distribution over the anionic sites.^[30] The successful incorporation of nitrogen has been proved by

complementary experimental analysis (*vide infra*). Therefore, the unusually high local symmetry of nitrogen environments in these systems is not fully satisfied in NdTiO₂N.[33]

3.2. Experimental electronic structure

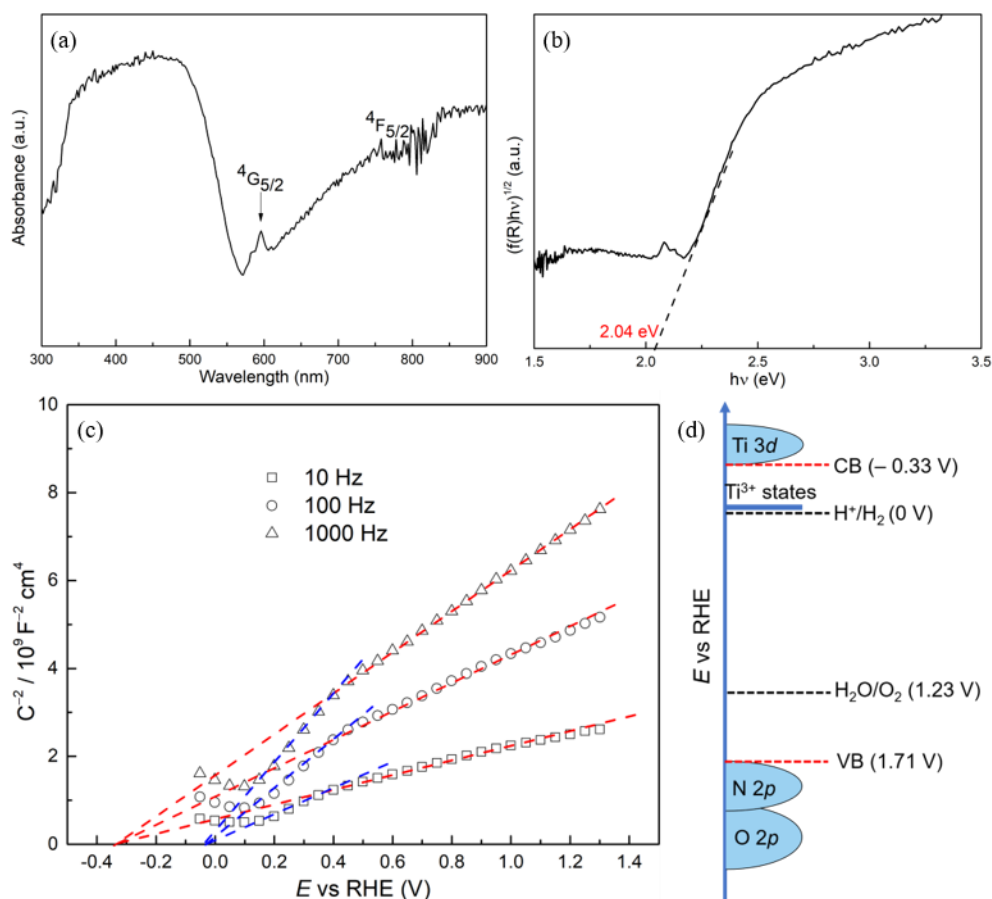


Fig. 3. UV-vis diffuse reflectance spectra of NdTiO₂N (a) and the corresponding Tauc plot (b); (c) Mott–Schottky plots for the FTO/NdTiO₂N electrode recorded at various frequencies in 1 M NaOH electrolyte (pH 13.6) under dark condition and (d) the band structure diagram of NdTiO₂N including Ti³⁺ states.

UV-vis diffuse reflectance spectra depicted in Fig. 3a were used to analyze the optical property of NdTiO₂N. A clear absorption edge at approximately 610 nm was confirmed, which is characteristic for NdTiO₂N. The background absorption (tail) in the infrared region indicates the presence of Ti³⁺ species originated from partial reduction Ti⁴⁺. [22,34] However, it is not possible to determine based on the IR analysis

the quantitative $\text{Ti}^{3+}/\text{Ti}^{4+}$ ratio. The phenomenon is more common occurring for niobium- and titanium-based oxynitrides than for tantalum-based oxynitrides because of the higher chemical stability of Ta^{5+} compared to Nb^{5+} and Ti^{4+} . [22,35–37] Another weak feature with respect to ${}^4G_{5/2}$ and ${}^4F_{5/2}$ f-f transitions on Nd^{3+} was also observed. The E_g was determined to be 2.04 eV by the Tauc-plot derived (Fig. 3b) from the UV-vis spectra, close to the previously reported value 2.1 eV for NdTiO_2N . [22]

It is generally known that the flat band potential (V_f) can be estimated via Mott–Schottky Eq. (1): [38]

$$\frac{1}{C^2} = \frac{2}{e_0 \varepsilon \varepsilon_0 N_d} \left(V - V_f - \frac{k_B T}{e_0} \right) \quad (1)$$

where C is the interfacial capacitance, N_d the number of donors, V the applied voltage, e_0 is the electronic charge, ε is the dielectric constant of the semiconductor, and ε_0 is the permittivity of free space, k_B is Boltzmann’s constant, T the absolute temperature. Therefore, the potential V_f can be obtained by extrapolation of the linear portion to the x-axis intercept from the plot of (differential capacitance)⁻² against the electrode potential. The Mott–Schottky plots measured at 10, 100 and 1000 Hz are presented in Fig. 3c. The sample developed positive slopes in plots as expected for n-type semiconductors. The capacitances were found to be frequency-dependent, revealing Fermi level pinning due to a midgap state. [39] The V_f was determined to be –0.33 V vs RHE from Fig. 3c, which is very close to LaTiO_2N at –0.37 vs RHE. [40]. It is interesting to note that secondary linearity portions (blue dashed lines) in the plots can be seen. In connection to the UV-vis absorption discussion, the secondary linearity portions were likely caused by shallow Ti^{3+} defects near to the conduction band. [34,41–44] The sub-band originated from shallow Ti^{3+} states and was estimated to be centered at –0.03 V vs RHE, slightly above the reduction potential of water. In combination with the UV-vis analysis, the position of both CB minimum and VB maximum are therefore

located approximately at -0.33 V vs RHE and 1.71 V vs RHE, respectively. The band structure diagram of NdTiO_2N including Ti^{3+} states is depicted in Fig. 3d, together with the reduction and oxidation potentials of water. The band positions of NdTiO_2N make it theoretically suitable for overall water splitting on a single absorber.

3.3. Calculated electronic structure

As the counterpart of experimental analysis, we performed theoretical investigations at the DFT level to elaborate more details of the electronic structure for the title compound. Three crystal structures with the same chemical compositions, but different N/O distributions were first created (Fig. 4a) and the corresponding lattice parameters and volumetric data are presented in Table S1. Thermodynamically, the one that possesses the lowest energy are much more likely to approach the experimental structure (Type 2, two nitrogen atoms in *cis*-type configuration) given thermodynamical control. The structure configuration therefore was used for further electronic structure calculation. The electronic band structure was calculated along the high-symmetry path “ $\Gamma(0, 0, 0) - X(\frac{1}{2}, 0, 0) - M(\frac{1}{2}, \frac{1}{2}, 0) - \Gamma(0, 0, 0)$ ”. The result produced by using the SCAN and HSE06 functionals are depicted in Fig. S1 and Fig. 4b, respectively, in combination with its density of states (DOS).[45] Note that due to the strong correlation for Nd 4f electrons, large self-interaction error occurs when these 4f electrons are treated as valence electrons. Indeed, it falsely describes the NdTiO_2N as metallic, while experiments confirm it to be semiconducting.[46] Therefore, we used a pseudopotential which treats the 4f electrons (orbitals) as core, accounting for their strong contraction. A direct band gap of 1.36 eV at the Γ point was obtained with SCAN, slightly smaller than the experimental 2.04 eV. After having including the Hartree–Fock exact exchange contribution (HSE06),[47] it leads to a wider band gap of 2.27 eV, in good agreement with the estimated experimental result. The additional calculation on Type 1

configuration, in which the N and O atoms have different local positions with Type 2 structure, yielded a band gap value of 1.99 eV (Fig. 4c), consistent with previous reports. [19] From its projected density of states (DOS), one can also observe that the valence bands are predominantly of N 2p and O 2p character, while the conduction bands are of Ti 3d character.

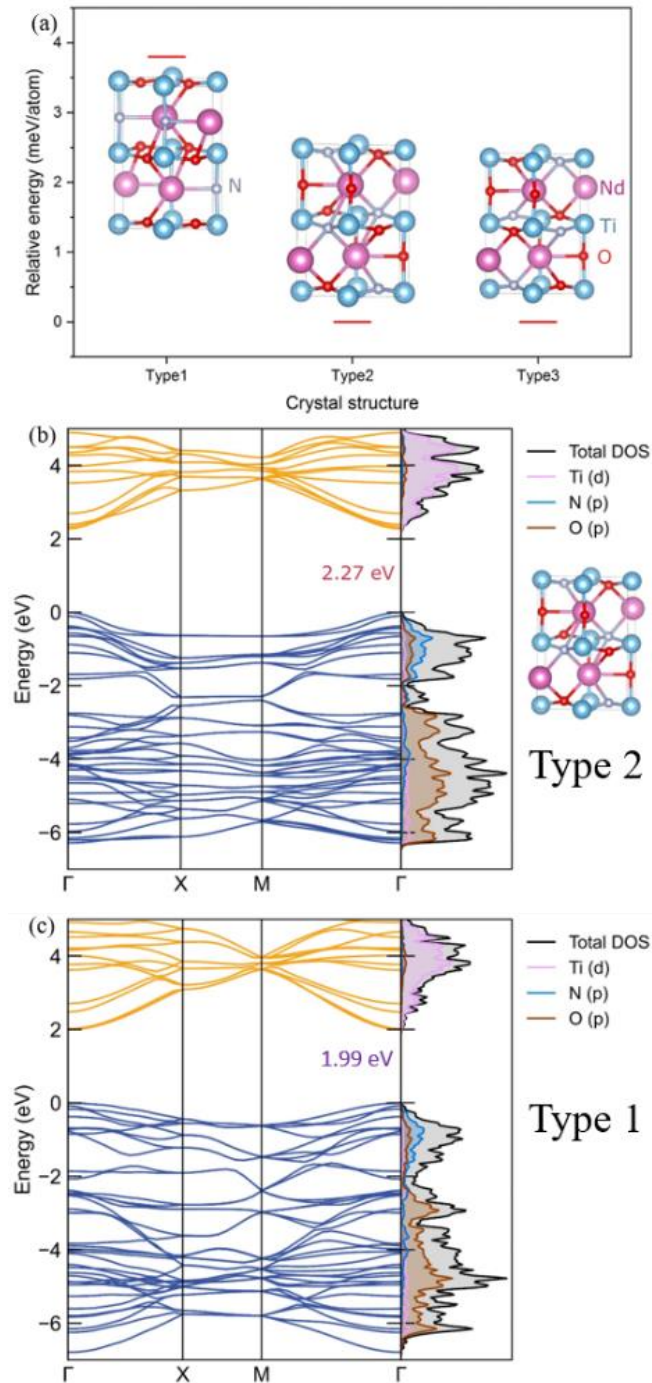


Fig. 4. (a) Three simulated structures for NdTiO_2N composition, with different kinds

of N/O distributions. The energies are relative to Type 2, the one that possesses the lowest energy. Type 2 is used for further electronic structure calculation; (b) the electronic band structure and projected density of states using HSE06 functional. The Fermi level is set to zero. The electronic band gap is calculated to be 2.27 eV; (c) electronic band structure and projected density of states with Type 1 configuration.

3.4. Characterization of photoanodes

Fig. 5a shows the SEM image of NdTiO_2N particles assembled as thin films on FTO. NdTiO_2N particles were estimated to be around 200 nm in diameter with irregular shapes. After post-necking with Nb_2O_5 and CoO_x overlayers, the particles were maintained in the original shapes (Fig. 5b). Eminently, the interconnectivity of particles was clearly improved to enable enhanced charge transfer.

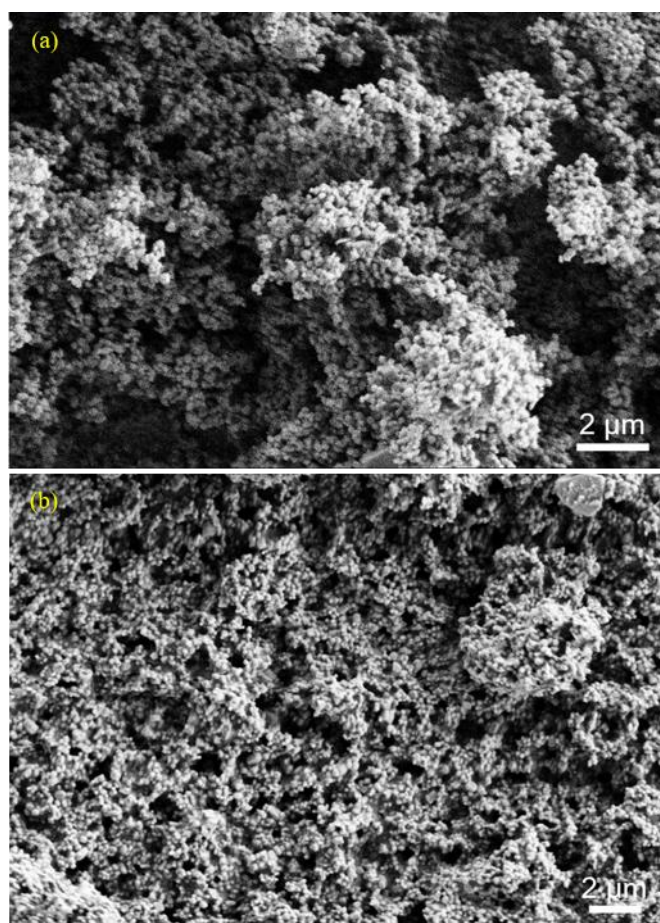


Fig. 5. SEM images of FTO/NdTiO₂N photoanodes (a) before and (b) after Nb₂O₅ and CoO_x post-modification.

The surface characterization technique XPS was employed to analyze the composition on the as-prepared composite FTO/NdTiO₂N/Nb₂O₅/CoO_x electrode. The collected spectra of the active phases (Co 2p, Nb 3d, Ti 2p, N 1s and Nd 4d) are presented in Fig. 6 and Fig. S2. Analyzing the structure of the electrode from outermost layers introduced by the subsequent covering FTO substrate, we find a cobalt phase with a chemical nature revealed by the XPS Co 2p spectrum (Fig. 6a). The characteristic doublet of Co 2p_{3/2} (780.2 eV) and Co 2p_{1/2} (795.5 eV) with spin-orbit splitting of 15.3 eV and no clear satellite structure confirms the presence of OER cocatalyst CoO_x with the dominant role of low-spin Co³⁺. [48] In turn, in the XPS Nb 3d spectrum the positions of the spin-orbit 3d_{5/2} (207.1 eV) and 3d_{3/2} (209.9 eV) components as well as symmetric peak shapes indicate the formation of a Nb₂O₅ phase (Fig. 6b) which can be related to the photoabsorber particles. [49] The core component of the studied semiconducting material is NdTiO₂N and the analyzed elements were analyzed on the basis of the XPS Ti 2p, N 1s and Nd 4d spectra (Fig. 6c, d and Fig. S2). The full width at half maximum (FWHM) of the Ti 2p_{3/2} and Ti 2p_{1/2} peaks are high enough to suggest the presence of Ti in various chemical environments. This is understandable due to the incorporation of Ti⁴⁺ into the NdTiO₂N oxynitride structure. The Ti 2p_{3/2} photoemission at 458.4 eV (with corresponding the Ti 2p_{1/2} component at 463.9 eV) is attributed to Ti in Ti-O bonds, while that at 457.3 eV (Ti 2p_{1/2} at 462.4 eV) is assigned to Ti in N-Ti-O bonds. [50] These results suggest Ti⁴⁺ cations locating in TiO_{6-x}N_x octahedra. Two peaks of N 1s spectra located at 395.8 eV and 400.1 eV were observed (Fig. 6d); similar pair peaks have been reported for N-doped TiO₂ and (La, Sr)TiO₂N. [51,52] The peak at binding energy of 395.8 eV indicates the incorporation of N into the metal oxynitride

lattice. The peak at higher binding energy of 400.1 eV can be attributed to either chemisorbed molecular N₂ on the surface or atomic β-N of TiN.[51,52] The exact interpretation of the Nd 3d region is troublesome due to the overlapping O KLL peaks. Therefore, we decided to use the less frequently analyzed, but more easily interpreted Nd 4d spectrum. The 4d_{5/2} photoemission observed at 121.9 eV clearly confirms neodymium presents in Nd³⁺ state (Fig. S2).[53,54]

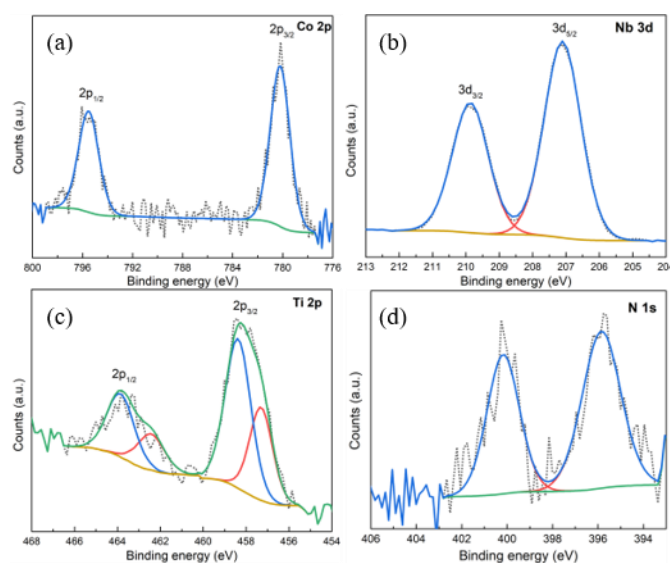


Fig. 6. XPS analysis on Co 2p (a), Nb 3d (b), Ti 2p (c) and N 1s (d) spectra of the FTO/NdTiO₂N/Nb₂O₅/CoO_x electrode.

3.5. Evaluation of photoelectrochemical properties

Although NdTiO₂N has the capability of absorbing wide range of visible light, the photoelectrode fabricated by means of EPD offered negligible photoresponse upon chopped irradiation (Fig. 7a). The low PEC performance of EPD-based photoelectrodes has been ascribed to the weak adhesion to the substrate and low interparticular electric conductivity.[37,55] A post-necking treatment step was thus applied to the as-prepared particle-based NdTiO₂N thin film by hydrolysis of NbCl₅ ethanol solution forming a thin Nb₂O₅ networking layer. As a consequence, the modified FTO/NdTiO₂N/Nb₂O₅ electrode yielded noticeable anodic photocurrent comparing to as-deposited

FTO/NdTiO₂N photoelectrode. It should be mentioned that similar effects have been observed on Pb₂Ti₄O₉F₂, Pb₂Ti₂O_{5.4}F_{1.2} and TaON particle-based thin film photoanode by modifying with Ta₂O₅ or TiO₂ deriving from TaCl₅ or TiCl₄. [15,23,56]

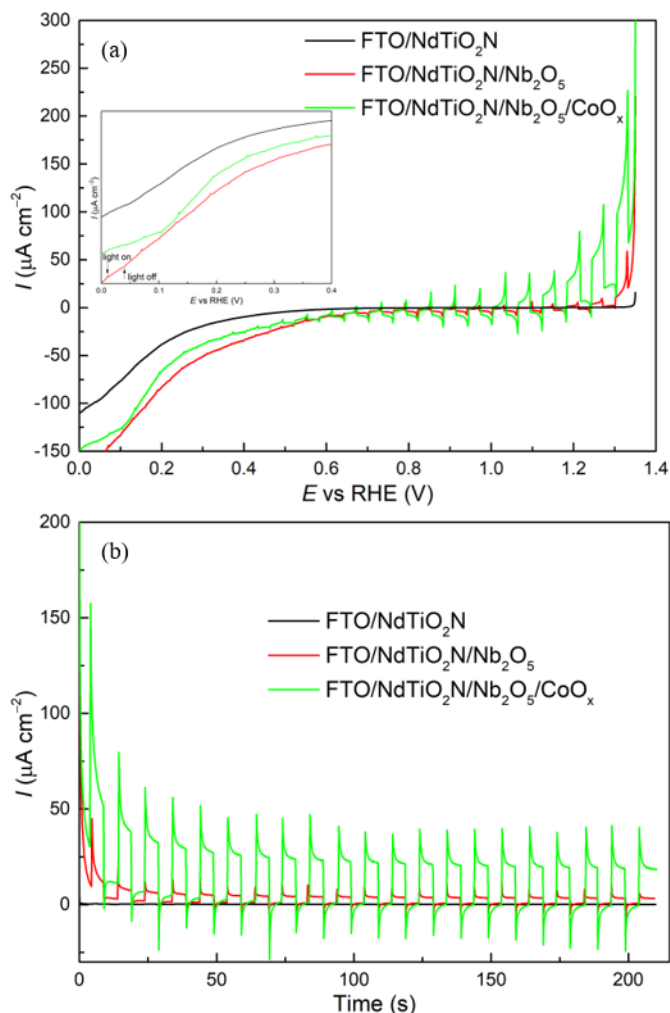


Fig. 7. (a) LSV curves of FTO/NdTiO₂N photoanode and the ones with sequentially Nb₂O₅ and CoO_x overlayers at a scan rate of 10 mV s⁻¹, inset shows the enlarged range between 0 V to 0.4 V vs RHE; (b) CA curves of FTO/NdTiO₂N photoanode and the ones with sequentially Nb₂O₅ and CoO_x overlayers at constant potential of 1.23 V vs RHE. Measurements were performed in 1 M NaOH electrolyte (pH 13.6) under interrupted AM 1.5G illumination (100 mW cm⁻²).

Since bare n-type semiconducting photoanodes tend to suffer from poor surface

water oxidation kinetics,[57,58] the photoexcited holes could thus accumulate at the surface and lead to photocorrosion.[59,60] The photocurrent density of the FTO/NdTiO₂N/Nb₂O₅ photoanode in conjunction with a known OER cocatalyst i.e. CoO_x was compared and presented in Fig. 7a. The photocurrent was improved considerably because of enhanced reaction kinetics and efficient utilization of the photogenerated holes reaching the electrode surface for water oxidation,[61] and a final photocurrent density of ca. 60 μA cm⁻² was developed at 1.23 V vs RHE. The photoresponse begins at very negative onset potential close to 0 V vs RHE (Fig. 7a, inset), profiting from its negative flat band potential. The post-amelioration effect of Nb₂O₅ and CoO_x overlayers was also reflected in the CA curves measured at constant potential of 1.23 V vs RHE (Fig. 7b). Both the LSV and CA curves exhibit obvious spikes caused by processes at the semiconductor surface upon switching illumination.[62,63]

3.6. Mechanism of activation

Besides the direct evidence provided by SEM in Fig. 5, additional electrochemical analytic techniques were carried out to reveal the reasons of the enhanced PEC performance induced by post-modification. EIS measurements were performed to evaluate the electrical properties of NdTiO₂N photoanode before and after modification with Nb₂O₅ and CoO_x. As presented in Fig. 8, the Nb₂O₅ modified FTO/NdTiO₂N photoanode exhibited much diminished arc radius of the semi-circular Nyquist plot, evidencing that the thin Nb₂O₅ network and the altered adhesion could reduce the charge transfer resistance. The charge transport properties were further ameliorated when decorating with a OER cocatalyst CoO_x (Fig. 8). The CoO_x decoration was supposed to accelerate the utilization of surface photogenerated holes to oxidize water, concurrently inducing extraction of deep charge carriers.[64] Thus, improvement PEC

performance was achieved in Fig. 7.

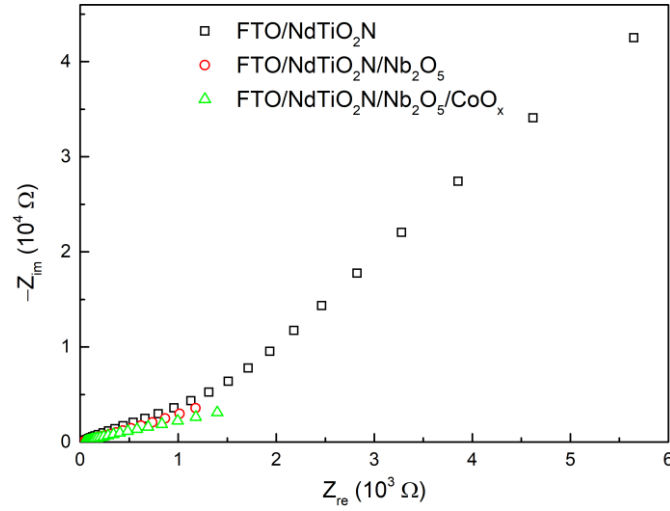


Fig. 8. Nyquist plots for FTO/NdTiO₂N photoanodes before and after modification with Nb₂O₅ and CoO_x measured at 1.0 V vs RHE under AM 1.5G illumination and at the frequency range of 20 kHz to 0.2 Hz.

Comparative analysis of Mott–Schottky plots were conducted on the modified FTO/NdTiO₂N photoanode. The flat band potential related to band bending were negatively shifted slightly as shown in Fig. 9, indicating enlarged band bending at the electrode/electrolyte interface which facilitating charge separation and transfer. The charge recombination at the interface also can be suppressed owing to negative flat band potential blocking electrons.[65] Another illustrious features of these Mott–Schottky plots are the decreasing slopes after post-treatment. The donor concentration is inversely proportional to the Mott–Schottky plot slope according to the following Eq. (2):[39]

$$N_d = \frac{2}{e_0 \epsilon \epsilon_0} \left[d \left(\frac{1}{c^2} \right) / dV \right]^{-1} \quad (2)$$

Though the qualitative N_d cannot be obtained due to the unknown dielectric constant ϵ of NdTiO₂N, the N_d was strongly increased by means of Nb₂O₅ treatment. The augmented value of N_d awakened the FTO/NdTiO₂N from negligible photoresponse (Fig. 7). A cocatalyst CoO_x modification raised the N_d slightly further,

but the photocurrent was significantly advanced. These were ascribed to prolonged lifetime and boosted charge separation.

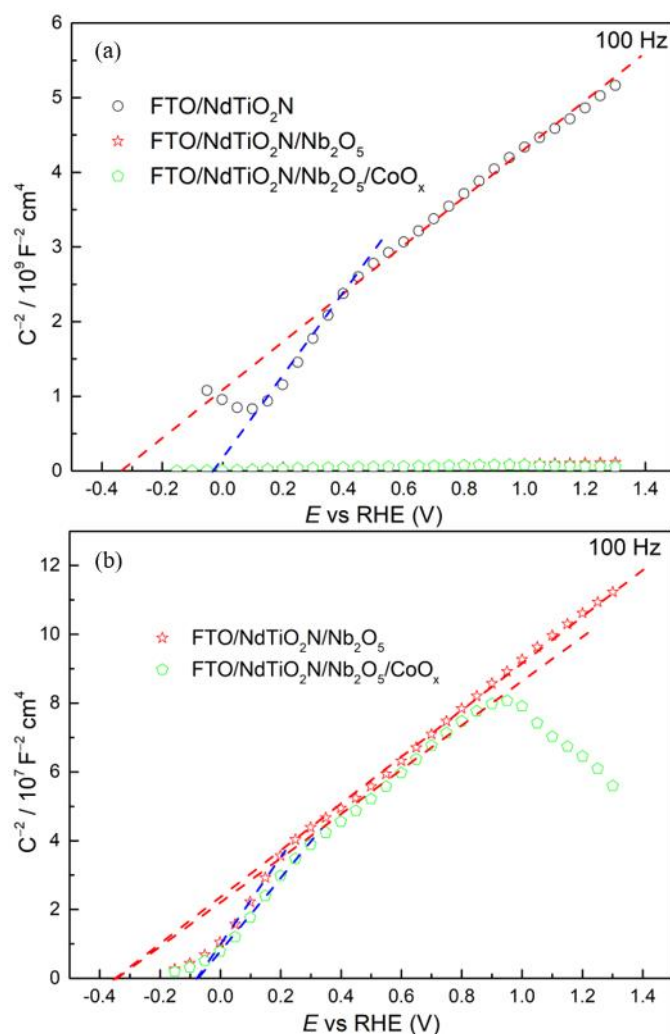


Fig. 9. (a) Mott–Schottky plots for the FTO/NdTiO₂N photoanode and the ones with sequentially Nb₂O₅ and CoO_x overlayers recorded at 100 Hz in 1 M NaOH electrolyte (pH 13.6) under dark condition. (b) Magnification of the same plot (note the different y-axis).

To probe the CoO_x effect in more detail, complementary transient photocurrent (TPC) measurements were carried out and are depicted in Fig. 10a. After deposition of the CoO_x cocatalyst, the greater initial anodic photocurrent spike, which originated from separation of photogenerated electron-hole pairs at the electrode/electrolyte interface,[66] indicated that holes can be captured by the new active sites for water

oxidation. The FTO/NdTiO₂N/Nb₂O₅/CoO_x photoanode also had remarkable longer photocurrent decay time than that of FTO/NdTiO₂N/Nb₂O₅, which can be attributed to the efficient separation and transfer of photogenerated charges. A cathodic current peak was observed upon turning off the light, and the current was restored to the initial dark level. The higher amount of cathodic charge was consistent with the longer photocurrent decay time.[67]

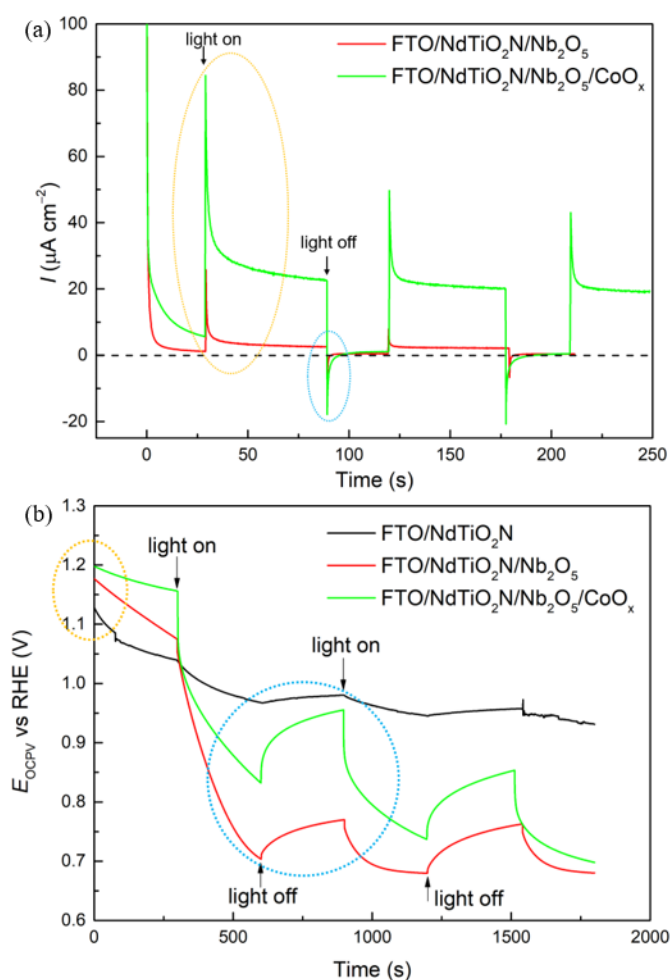


Fig. 10. (a) Transient photocurrent (TPC) measurements for the photoanode of FTO/NdTiO₂N/Nb₂O₅ and FTO/NdTiO₂N/Nb₂O₅/CoO_x in 1 M NaOH electrolyte and (b) OCPV curves measured with for the FTO/NdTiO₂N photoanode and the ones with sequentially Nb₂O₅ and CoO_x overlayers in 1 M NaOH electrolyte without hole scavenger.

Since surface states could lead to Fermi level pinning at the surface,[68] ideal photoanodes with no Fermi level pinning would expect to produce an open circuit potential under dark condition (OCP_{dark}) close to 1.23 V vs RHE.[69] As marked with orange oval in Fig. 10b, the OCP_{dark} of bare FTO/NdTiO₂N positively shifted from 1.12 V to 1.18 V vs RHE due to altered surface trap states by necking with the Nb₂O₅ thin overlayer. Grafting the OER catalyst CoO_x diminished the Fermi level pinning effect further; thus the equilibrium potential OCP_{dark} was pressed toward the water oxidation potential.[67] For photoelectrodes, the difference between open circuit potential in dark and light, i.e. OCPV, is crucial. Incremental OCPV with sequentially Nb₂O₅ and CoO_x overlayers was observed in Fig. 10b (blue circle), which is equal to a higher driving force toward water oxidation and therewith enhanced photocurrent (Fig. 7).[70,71]

4. Conclusions

In summary, the properties of one member of the titanium-based quaternary oxynitrides, i.e. NdTiO₂N, were investigated. The band gap of the mixed-anion compound NdTiO₂N was determined to be 2.04 eV, only slightly different from the theoretical value calculated at DFT level. Mott–Schottky measurements demonstrate that NdTiO₂N possesses a relative negative CB edge located at around –0.33 vs RHE, more negative than the potential of water reduction. The VB edge was thus proposed to be 1.71 V vs RHE, indicating a band structure beyond the reduction and oxidation potentials of water. This makes the title compound theoretically able to perform overall water splitting on a single absorber. Furthermore, the solid-state ¹⁴N NMR signals of NdTiO₂N could not be detected, confirming that NdTiO₂N is not exactly stoichiometric in comparison to structurally-related metal oxynitrides.

Examining the particle-based bare photoanode did not exhibit noticeable photocurrent. Exceptionally, a noteworthy augmented photocurrent was achieved after

subjecting to postdeposition of Nb₂O₅ and CoO_x overlayer. SEM, EIS and Mott-Schottky analysis evidenced that the thin Nb₂O₅ overlayer could enhance the connections between the NdTiO₂N particles and thus increased the charge carrier concentration significantly facilitating charge transfer. OCPV and TPC measurements confirmed that the OER cocatalyst CoO_x overlayer can ameliorate the surface states and accelerate the utilization of surface photogenerated holes, therefore extract deeper holes and prolonging their lifetime. Our results highlight the capability of NdTiO₂N as photoactive material with wide visible light absorption edge for PEC water splitting. Further efforts on one-dimensional nanostructure fabrication should improve the PEC efficiency by decoupling charge carrier transport from light absorption.

Acknowledgments

A. S. would like to thank Vinnova, the Swedish innovation agency, for financial support (project: C1Bio 2019-03174). We thank Xianji Qiao for helpful discussions and Birgit Hahn for SEM measurements. Z.M. would like to thank the China Scholarship Council for a Ph.D. scholarship. K.C. gratefully thanks the financial support from the Alexander von Humboldt Foundation. The XPS measurements were carried out with the equipment purchased with the financial support of the European Regional Development Fund in the framework of the Polish Innovation Operational Program (contract no. POIG.02.01.00-12-023/08). The simulation work was supported by the IT center of RWTH Aachen University under grant JARA-HPC (JARA0179).

References

- [1] C. Lu, Z. Ma, J. Jäger, T.M. Budnyak, R. Dronskowski, A. Rokicińska, P. Kuśtrowski, F. Pammer, A. Slabon, *ACS Appl. Mater. Interfaces* 12 (2020) 29173–29180.
- [2] J. Hogerwaard, I. Dincer, G.F. Naterer, *Energy Convers. Manag.* 207 (2020) 112541.
- [3] M. Volokh, G. Peng, J. Barrio, M. Shalom, *Angew. Chem. Int. Ed.* 58 (2019)

- 6138–6151.
- [4] K. Sivula, R. van de Krol, *Nat. Rev. Mater.* 1 (2016) 15010.
 - [5] H. Kageyama, K. Hayashi, K. Maeda, J.P. Attfield, Z. Hiroi, J.M. Rondinelli, K.R. Poeppelmeier, *Nat. Commun.* 9 (2018) 772.
 - [6] P.-H. Chien, J.K. Harada, H. Liu, S. Patel, C. Huang, J.M. Rondinelli, K.R. Poeppelmeier, Y.-Y. Hu, *Chem. Mater.* 32 (2020) 5715–5722.
 - [7] U. Dang, W. Zaheer, W. Zhou, A. Kandel, M. Orr, R.W. Schwenz, G. Laurita, S. Banerjee, R.T. Macaluso, *Chem. Mater.* 32 (2020) 7404–7412.
 - [8] J. Oró-Solé, I. Fina, C. Frontera, J. Gàzquez, C. Ritter, M. Cunqueiro, P. Loza-Alvarez, S. Conejeros, P. Alemany, E. Canadell, J. Fontcuberta, A. Fuertes, *Angew. Chem. Int. Ed.* (2020), DOI: 10.1002/anie.202006519.
 - [9] S. Balaz, S.H. Porter, P.M. Woodward, L.J. Brillson, *Chem. Mater.* 25 (2013) 3337–3343.
 - [10] M. Davi, A. Drichel, M. Mann, T. Scholz, F. Schrader, A. Rokicinska, P. Kustrowski, R. Dronskowski, A. Slabon, *J. Phys. Chem. C* 121 (2017) 26265–26274.
 - [11] Z. Chen, M. Löber, A. Rokicińska, Z. Ma, J. Chen, P. Kuśtrowski, H.-J. Meyer, R. Dronskowski, A. Slabon, *Dalt. Trans.* 49 (2020) 3450–3456.
 - [12] J. Seo, T. Hisatomi, M. Nakabayashi, N. Shibata, T. Minegishi, M. Katayama, K. Domen, *Adv. Energy Mater.* 8 (2018) 1800094.
 - [13] A. Kubo, G. Giorgi, K. Yamashita, *Chem. Mater.* 29 (2017) 539–545.
 - [14] Y. Pihosh, V. Nandal, T. Minegishi, M. Katayama, T. Yamada, K. Seki, M. Sugiyama, K. Domen, *ACS Energy Lett.* 5 (2020) 2492–2497.
 - [15] N. Hirayama, H. Nakata, H. Wakayama, S. Nishioka, T. Kanazawa, R. Kamata, Y. Ebato, K. Kato, H. Kumagai, A. Yamakata, K. Oka, K. Maeda, *J. Am. Chem. Soc.* 141 (2019) 17158–17165.
 - [16] Y. Bai, L. Ye, T. Chen, L. Wang, X. Shi, X. Zhang, D. Chen, *ACS Appl. Mater. Interfaces* 8 (2016) 27661–27668.
 - [17] F. Yoshitomi, K. Sekizawa, K. Maeda, O. Ishitani, *ACS Appl. Mater. Interfaces* 7 (2015) 13092–13097.
 - [18] S.G. Ebbinghaus, H.P. Abicht, R. Dronskowski, T. Müller, A. Reller, A. Weidenkaff, *Prog. Solid State Chem.* 37 (2009) 173–205.
 - [19] H. Wolff, R. Dronskowski, *J. Comput. Chem.* 29 (2008) 2260–2267.
 - [20] W.-J. Chun, A. Ishikawa, H. Fujisawa, T. Takata, J.N. Kondo, M. Hara, M. Kawai, Y. Matsumoto, K. Domen, *J. Phys. Chem. B* 107 (2003) 1798–1803.
 - [21] S. Akiyama, M. Nakabayashi, N. Shibata, T. Minegishi, Y. Asakura, M. Abdulla-Al-Mamun, T. Hisatomi, H. Nishiyama, M. Katayama, T. Yamada, K. Domen, *Small* 12 (2016) 5468–5476.
 - [22] S.H. Porter, Z. Huang, S. Dou, S. Brown-Xu, A.T.M. Golam Sarwar, R.C. Myers, P.M. Woodward, *Chem. Mater.* 27 (2015) 2414–2420.
 - [23] K. Maeda, N. Hirayama, H. Nakata, H. Wakayama, K. Oka, *J. Phys. Chem. C* 124 (2020) 1844–1850.
 - [24] G. Kervern, G. Pintacuda, L. Emsley, *Chem. Phys. Lett.* 435 (2007) 157–162.
 - [25] T. Hwang, P.C.M. van Zijl, M. Garwood, *J. Magn. Reson.* 133 (1998) 200–203.

- [26] G. Kresse, J. Furthmüller, *Phys. Rev. B* 54 (1996) 11169–11186.
- [27] J. Sun, A. Ruzsinszky, J. Perdew, *Phys. Rev. Lett.* 115 (2015) 036402.
- [28] D. Abeyasinghe, S.E. Skrabalak, *ACS Energy Lett.* 3 (2018) 1331–1344.
- [29] N. Ishizawa, K. Ninomiya, T. Sakakura, J. Wang, *Acta Crystallogr. Sect. E Struct. Reports* 69 (2013) i19–i19.
- [30] S.J. Clarke, B.P. Guinot, C.W. Michie, M.J.C. Calmont, M.J. Rosseinsky, *Chem. Mater.* 14 (2002) 288–294.
- [31] Y.S. Reddy, P. Kistaiah, C. Vishnuvardhan Reddy, *Rare Met.* 33 (2014) 166–170.
- [32] L.K. Joseph, K.R. Dayas, S. Damodar, B. Krishnan, K. Krishnankutty, V.P.N. Nampoori, P. Radhakrishnan, *Spectrochim. Acta Part A Mol. Biomol. Spectrosc.* 71 (2008) 1281–1285.
- [33] Z. Ma, R. Dronskowski, A. Slabon, A. Jaworski, *ChemRxiv* (2020), DOI: 10.26434/chemrxiv.12902594.v1.
- [34] H.A. Seibel II, P. Karen, T.R. Wagner, P.M. Woodward, *J. Mater. Chem.* 19 (2009) 471–477.
- [35] X. Wang, T. Hisatomi, J. Liang, Z. Wang, Y. Xiang, Y. Zhao, X. Dai, T. Takata, K. Domen, *J. Mater. Chem. A* 8 (2020) 11743–11751.
- [36] Y.-I. Kim, P.M. Woodward, K.Z. Baba-Kishi, C.W. Tai, *Chem. Mater.* 16 (2004) 1267–1276.
- [37] Z. Ma, A. Jaworski, J. George, A. Rokicinska, T. Thersleff, T.M. Budnyak, G. Hautier, A.J. Pell, R. Dronskowski, P. Kuśtrowski, A. Slabon, *J. Phys. Chem. C* 124 (2020) 152–160.
- [38] K. Gelderman, L. Lee, S.W. Donne, *J. Chem. Educ.* 84 (2007) 685.
- [39] Z. Ma, O. Linnenberg, A. Rokicinska, P. Kustrowski, A. Slabon, *J. Phys. Chem. C* 122 (2018) 19281–19288.
- [40] L. Mao, X. Cai, H. Gao, X. Diao, J. Zhang, *Nano Energy* 39 (2017) 172–182.
- [41] A. Ammari, M. Trari, *Colloids Surfaces A Physicochem. Eng. Asp.* 561 (2019) 178–186.
- [42] P.C. Harikesh, B. Wu, B. Ghosh, R.A. John, S. Lie, K. Thirumal, L.H. Wong, T.C. Sum, S. Mhaisalkar, N. Mathews, *Adv. Mater.* 30 (2018) 1802080.
- [43] K. Chang-Ha, P. Su-II, L. Eung-Jo, *Mater. Lett.* 10 (1991) 387–391.
- [44] J. Schoonman, *J. Electrochem. Soc.* 128 (1981) 1154.
- [45] A. M Ganose, A. J Jackson, D. O Scanlon, *J. Open Source Softw.* 3 (2018) 717.
- [46] A. Slabon, C. Mensing, C. Kubata, E. Cuervo-Reyes, R. Nesper, *Angew. Chem. Int. Ed.* 52 (2013) 2122–2125.
- [47] K. Chen, R. Dronskowski, *J. Phys. Chem. A* 123 (2019) 9328–9335.
- [48] D. Barreca, A. Gasparotto, O.I. Lebedev, C. Maccato, A. Pozza, E. Tondello, S. Turner, G. Van Tendeloo, *CrystEngComm* 12 (2010) 2185.
- [49] B.R. King, H.C. Patel, D.A. Gulino, B.J. Tatarchuk, *Thin Solid Films* 192 (1990) 351–369.
- [50] F. Meng, Z. Hong, J. Arndt, M. Li, M. Zhi, F. Yang, N. Wu, *Nano Res.* 5 (2012) 213–221.
- [51] C. Wang, Q. Hu, J. Huang, L. Wu, Z. Deng, Z. Liu, Y. Liu, Y. Cao, *Appl. Surf. Sci.* 283 (2013) 188–192.

- [52] Y. Masuda, R. Mashima, M. Yamada, K. Ikeuchi, K. Murai, G.I.N. Waterhouse, J.B. Metson, T. Moriga, *J. Ceram. Soc. Japan* 117 (2009) 76–81.
- [53] B. Trujillo-Navarrete, F. Paraguay-Delgado, S. Pérez-Sicairos, *Appl. Phys. A* 126 (2020) 592.
- [54] W. Li, A.I. Frenkel, J.C. Woicik, C. Ni, S.I. Shah, *Phys. Rev. B* 72 (2005) 155315.
- [55] M. Higashi, K. Domen, R. Abe, *Energy Environ. Sci.* 4 (2011) 4138.
- [56] S.S. Gujral, A.N. Simonov, M. Higashi, R. Abe, L. Spiccia, *ChemElectroChem* 2 (2015) 1270–1278.
- [57] J.B. Sambur, T.-Y. Chen, E. Choudhary, G. Chen, E.J. Nissen, E.M. Thomas, N. Zou, P. Chen, *Nature* 530 (2016) 77–80.
- [58] N.T. Hahn, C.B. Mullins, *Chem. Mater.* 22 (2010) 6474–6482.
- [59] K. Oh, V. Dorcet, B. Fabre, G. Loget, *Adv. Energy Mater.* 10 (2020) 1902963.
- [60] Y. Kuang, Q. Jia, G. Ma, T. Hisatomi, T. Minegishi, H. Nishiyama, M. Nakabayashi, N. Shibata, T. Yamada, A. Kudo, K. Domen, *Nat. Energy* 2 (2017) 16191.
- [61] L. Liardet, J.E. Katz, J. Luo, M. Grätzel, X. Hu, *J. Mater. Chem. A* 7 (2019) 6012–6020.
- [62] M. Higashi, K. Domen, R. Abe, *J. Am. Chem. Soc.* 134 (2012) 6968–6971.
- [63] L. Pei, H. Wang, X. Wang, Z. Xu, S. Yan, Z. Zou, *Dalt. Trans.* 47 (2018) 8949–8955.
- [64] S.A. Lee, T.H. Lee, C. Kim, M.-J. Choi, H. Park, S. Choi, J. Lee, J. Oh, S.Y. Kim, H.W. Jang, *ACS Catal.* 10 (2020) 420–429.
- [65] J. Liang, N. Wang, Q. Zhang, B. Liu, X. Kong, C. Wei, D. Zhang, B. Yan, Y. Zhao, X. Zhang, *Nano Energy* 42 (2017) 151–156.
- [66] A. Hagfeldt, H. Lindström, S. Södergren, S.-E. Lindquist, *J. Electroanal. Chem.* 381 (1995) 39–46.
- [67] J.W. Moir, E. V. Sackville, U. Hintermair, G.A. Ozin, *J. Phys. Chem. C* 120 (2016) 12999–13012.
- [68] F. Le Formal, K. Sivula, M. Grätzel, *J. Phys. Chem. C* 116 (2012) 26707–26720.
- [69] C. Du, M. Zhang, J.-W. Jang, Y. Liu, G.-Y. Liu, D. Wang, *J. Phys. Chem. C* 118 (2014) 17054–17059.
- [70] Y. Liu, N. Guijarro, K. Sivula, *Helv. Chim. Acta* 103 (2020) e2000064.
- [71] K.-H. Ye, H. Li, D. Huang, S. Xiao, W. Qiu, M. Li, Y. Hu, W. Mai, H. Ji, S. Yang, *Nat. Commun.* 10 (2019) 3687.

Graphical Abstract

Structural properties of mixed-anion NdTiO_2N oxynitride were experimentally and theoretically investigated and examined for photoelectrochemical water oxidation owing to its narrow band gap but straddling the reduction and oxidation potentials of water.

